Biomaterials 112 (2017) 324–335

Contents lists available at ScienceDirect

Biomaterials

journal homepage: www.elsevier.com/locate/biomaterials

Oxygen-generating hybrid nanoparticles to enhance fluorescent/photoacoustic/ultrasound imaging guided tumor photodynamic therapy

Shi Gao [a, 1], Guohao Wang [b, 1], Zainen Qin [b], Xiangyu Wang [b], Guoqing Zhao [a, **], Qingjie Ma [a, ***], Lei Zhu [b, c, *]

[a] Department of Nuclear Medicine, China-Japan Union Hospital, Jilin University, Changchun, Jilin, 130033, China
[b] State Key Laboratory of Molecular Vaccinology and Molecular Diagnostics & Center for Molecular Imaging and Translational Medicine, School of Public Health, Xiamen University, Xiamen, 361005, China
[c] Department of Surgery, Emory University School of Medicine, Atlanta, GA, 30322, United States

ARTICLE INFO

Article history:
Received 3 October 2016
Received in revised form
18 October 2016
Accepted 19 October 2016
Available online 19 October 2016

Keywords:
Hypoxia
Oxygen generating
Image-guided therapy
Photodynamic therapy
Hyaluronic acid particles
Manganese dioxide nanoparticles

ABSTRACT

Photodynamic therapy (PDT) is a promising tumor treatment modality that can convert oxygen into cytotoxic singlet oxygen (SO) *via* photosensitizer to ablate tumor growth. However, the uncontrolled cancer cell proliferation during tumor development and the oxygen consumption during PDT always result in an insufficient oxygen level in tumors, which can adversely affect the PDT efficiency in turn. We designed an oxygen-generating PDT nanocomplex by encapsulating a manganese dioxide nanoparticle (MnO_2 NP) in an indocyanine green (ICG) modified hyaluronic acid nanoparticle (HANP) to overcome this limitation. Because of the excellent fluorescent and photoacoustic properties, the tumor accumulation of the ICG-HANP/MnO_2 (IHM) nanocomplex was monitored by fluorescent imaging and photoacoustic imaging after intravenous administration into the SCC7 tumor-bearing mouse model. Both high fluorescent and photoacoustic signals were detected and found peak at 6 h post-injection (tumor-muscle ratio: 4.03 ± 0.36 for fluorescent imaging and 2.93 ± 0.13 for photoacoustic imaging). In addition, due to the high reactivity of MnO_2 NP to H_2O_2, an unfavorable tumor cell metabolic, the oxygen content in the tumor is elevated 2.25 ± 0.07 times compared to that without IHM treatment as ultrasound imaging confirmed. After laser irradiation, significant tumor growth inhibition was observed in the IHM-treated group compared to the ICG-HANP-treated group, attributed to the beneficial oxygen-generating property of IHM for PDT. It is expected that the design of IHM will provide an alternative way of improving clinical PDT efficacy and will be widely applied in cancer theranostics.

Cancer is a major public health concern in most parts of the world [1,2]. Due to the high mortality rate and treatment costs, great efforts have been devoted to efficient cancer treatment approaches. Among the current cancer therapy strategies, photodynamic therapy (PDT) is a new non-invasive modality and is expected to surpass the traditional cancer treatment methods such as chemotherapy, radiotherapy, and surgery. For example, extensive preclinical studies are utilizing PDT to overcome classical drug resistance or escape pathways to improve the efficacy of many pharmaceuticals [3,4]. Encouragingly, PDT has been approved by United States Food and Drug Administration (FDA) for the treatment of patients with esophageal cancer, Barrett's esophagus, and non-small cell lung cancer [1]. In the process of PDT, an excited photosensitizer can undergo type I (electron transfer) or, in most cases, type II (energy transfer) reaction to produce reactive oxygen species (ROS) resulting an apoptosis or necrosis in exposed cells [5–7]. Specifically, type I reactions generate radical and radical anion species ($O_2^{\bullet -}$ or HO•), while type II reactions can produce singlet oxygen ($^1O_2$) *via* transferring energy to nearby oxygen molecules [7,8]. Obviously, the effect of type II PDT largely depends

* Corresponding author. Department of Surgery, Emory University School of Medicine, Atlanta, GA 30322, United States.
** Corresponding author.
*** Corresponding author.
E-mail addresses: zhaoguoqjlu@163.com (G. Zhao), maqingjiejlu@163.com (Q. Ma), lei.zhu@emory.edu (L. Zhu).
[1] These authors contributed equally to this manuscript.

http://dx.doi.org/10.1016/j.biomaterials.2016.10.030
0142-9612/

on the amount of oxygen in the tumor [9,10]. Unfortunately, as we know, most solid tumors are characterized by hypoxia [11], an inadequate oxygen supply that is caused by deteriorating microenvironments, abnormal blood vessels, and uncontrollable cancer cell proliferation [12]. Clinical studies have proven that the cells in hypoxia regions are prone to being resistant to radiotherapy and chemotherapy [11–13]. Additionally, it has been reported that PDT efficiency is significantly decreased or even diminished when O_2 pressure goes below 40 mmHg [14,15], which is usually lower than 15 mmHg in most types of tumors [11,13]. Therefore, the efficiency of PDT treatment for cancer is still limited and a new PDT strategy is highly desired.

Nanomedicine to ameliorate cancer's therapeutic effects has attracted great attention in recent years [16–19]. As far as PDT is concerned, various nanomaterial-PS complexes have been proposed to improve PS delivery efficiency and reduce PDT side effect [20], aiming to promote PDT applications in tumor treatment. For example, high PS loading nanoformulation, a tumor specific targeting nanoplatform, and hybrid tumor treatment nanocomposition have all been widely reported by many research groups, including us [20–23]. In addition, new PS with excellent photostability and biocompatibility was invented aiming to enhance PDT effects [24–26]. Although these investigations demonstrated promising PDT tumor ablation effects, the key constraint of PDT, low amounts of oxygen in the tumor, was not still lifted. So far, a few attempts have been reported for attenuating hypoxia in tumor milieu [27,28], many of which are developed by directly transporting oxygen molecules (O_2) by nanovehicles with finite oxygen loading capacity [1,29,30]. Improving oxygenation in the tumor to enhance PDT effect is still challenging.

Previous studies suggest that cancer cells normally produce more ROS, for example H_2O_2, than normal cells, because of the rapid metabolic activity in cancer cells [31,32]. Herein, by exploiting the high reactivity of manganese dioxide nanoparticles (MnO_2 NP) with H_2O_2 [33,34], we rationally designed an O_2 generating and tumor-targeted hybrid nanoparticle in order to improve tumor PDT efficiency (Fig. 1a). Specifically, indocyanine green (ICG) as a photosensitizer was covalently conjugated onto the surface of hyaluronic acid nanoparticles (HANP), achieving a near infrared (NIR) laser-activated photosensitizer (IHANP). Subsequently, MnO_2 NP was encapsulated into IHANP to improve the biocompatibility and tumor targetability. Importantly, the yielding MnO_2 NP complexed IHANP (IHM) can be internalized into tumor cells when binding with CD44 overexpressed on tumor cells *via* HANP [35,36]. After hyaluronidase degradation, released MnO_2 NP will react with H_2O_2, a massive tumor metabolite [32,37], to generate oxygen molecules that are vital for improving PDT efficacy. To optimize a therapeutic time window, we took advantage of the fluorescent and photoacoustic (PA) imaging property of ICG and monitored the tumor accumulation of IHM. In our complex, PA imaging can provide structural information of biological tissues such as blood vessel distribution in tumor, and fluorescent imaging is capable of offering complementary information of PA from whole body. Both of the imaging modalities will facilitate analyzing the *in vivo* behavior of IHM. Moreover, we also applied ultrasound/photoacoustic imaging technique to observe the generation of oxygen in tumor area, so that PDT can be initiated with abundant oxygen. As imaging suggested, a NIR laser was applied at 6 h post-injection of IHM when it peaked in tumor, converting oxygen into cytotoxic singlet oxygen (SO) *via* ICG for tumor ablation. Compared with control groups, an enhanced tumor ablation effect was observed after oxygen-evolving IHM facilitated PDT in SCC7 tumor mouse xerograph, and no recurrence was detected during our study. Collectively, IHM with excellent biocompatibility is able to a) effectively target tumor cells with CD44 as well as producing an enhanced permeability retention (EPR) effect; b) *in situ* generate O_2 to enhanced PDT efficacy; and c) ablate tumor growth with negligible side effects. Our results suggested the promise of IHM in image-guided cancer therapy and created an opportunity to improve PDT efficiency. It is expected that our new strategy may facilitate the translation of IHM into the clinic as a theranostic agent.

1. Results and discusstion

1.1. Preparation of IHM

Manganese dioxide nanoparticles (MnO_2 NP) were synthesized as reported [38,39] in the organic phase. The next day, a hedgehog-like ball of MnO_2 was obtained and the diameter was measured as 35 ± 2.5 nm (Fig. 1 and S1). Meanwhile, hyaluronic acid nanoparticles (HANPs) were prepared and functionalized with a near-infrared photosensitizer ICG (ex/em: 780/800 nm, Fig. S2) [20,40]. This photosensitizer-labeled HA nanoparticle was named as IHANP. Specifically, HANP is composed of the hydrophilic hyaluronic acid (HA) part and the hydrophobic 5β-chrolanic acid part. The yielding HANP is a yarn like nanoparticle with hydrophilic surface and hydrophobic cave inside. With NIR absorbance, it was expected that ICG could facilitate a relative deep tissue penetration of PDT. Due to the overexpression of CD44 in tumor cells and the tumor-enhanced permeability retention effect, IHANP can effectively accumulate in the tumor as an ideal nanocarrier [20,40]. To enrich the amount of oxygen in the tumor, hydrophobic MnO_2 was encapsulated into the hydrophobic caves in IHANP with high pressure homogenizer, forming a MnO_2/IHANP complex and denoted as IHM. In order to optimize the MnO_2 loading efficiency, IHM integrated with different MnO_2 and IHANP ratios (1:9, 1:4 and 2:3, w/w) were investigated (Table 1). It was found that the loading efficiency was highest (81.55% ± 3.31%) when the MnO_2 and IHANP ratio was 1:4 and this composition was applied throughout the study. Abundant oxygen was produced when IHM encountered H_2O_2 as shown in Fig. 1b, so we hypothesized that the oxygen would attenuate tumor hypoxia as well as increase the PDT efficiency. Compared to IHANP (180 ± 3.5 nm), IHM diameter increased to 239 ± 4.2 nm measured by transmission electron microscopy (TEM) and dynamic light scattering (DLS) due to the encapsulation of MnO_2 (Fig. 1c). To further confirm the construction of IHM, vis/UV/NIR absorbance spectrum of IHM was acquired. A broad distinctive peak was observed around the 350–375 nm range for MnO2 was observed due to the surface plasmon band [28,41]. Specific peaks from both MnO_2 and ICG were observed at 420 nm and 780 nm, respectively, suggesting the successful encapsulation of MnO_2 into IHANP. A slight red shift of absorbance spectrum from 780 nm to 800 nm of IHM was also observed, which could have been caused by the close interaction between the ICG dyes on IHM. In addition, emission wavelength was not found to change for both ICG and IHM, implying the fluorescent property of ICG was not affected after it was conjugated onto HANP (Fig. S3b). Although metal nanoparticles are reported can quench fluorescent signals [19], in this study MnO_2 is not able to quench ICG fluorescent signals. This is because MnO_2 only showed strong absorbance at around 400 nm (Fig. 1d), while emission of ICG is around 810 nm [20]. In addition, the crystal structure of manganese species was studied by the X-ray diffraction (XRD) in Fig. 1e. Significant XRD peaks were recorded in MnO_2 and IHM at $2\theta = 12.3, 24.3, 36.6$, and 65.7°, and could be well-assigned to the (001), (002), (100), and (110) planes of birnessite-type MnO_2, respectively [39]. All these data indicate that MnO_2 nanoparticle and IHM was successfully synthesized. In view of the strong photoacoustic (PA) effect of ICG, different concentrations of IHM were evaluated by the photoacoustic imaging system and no obvious PA signals changes were observed in the ICG-treated group

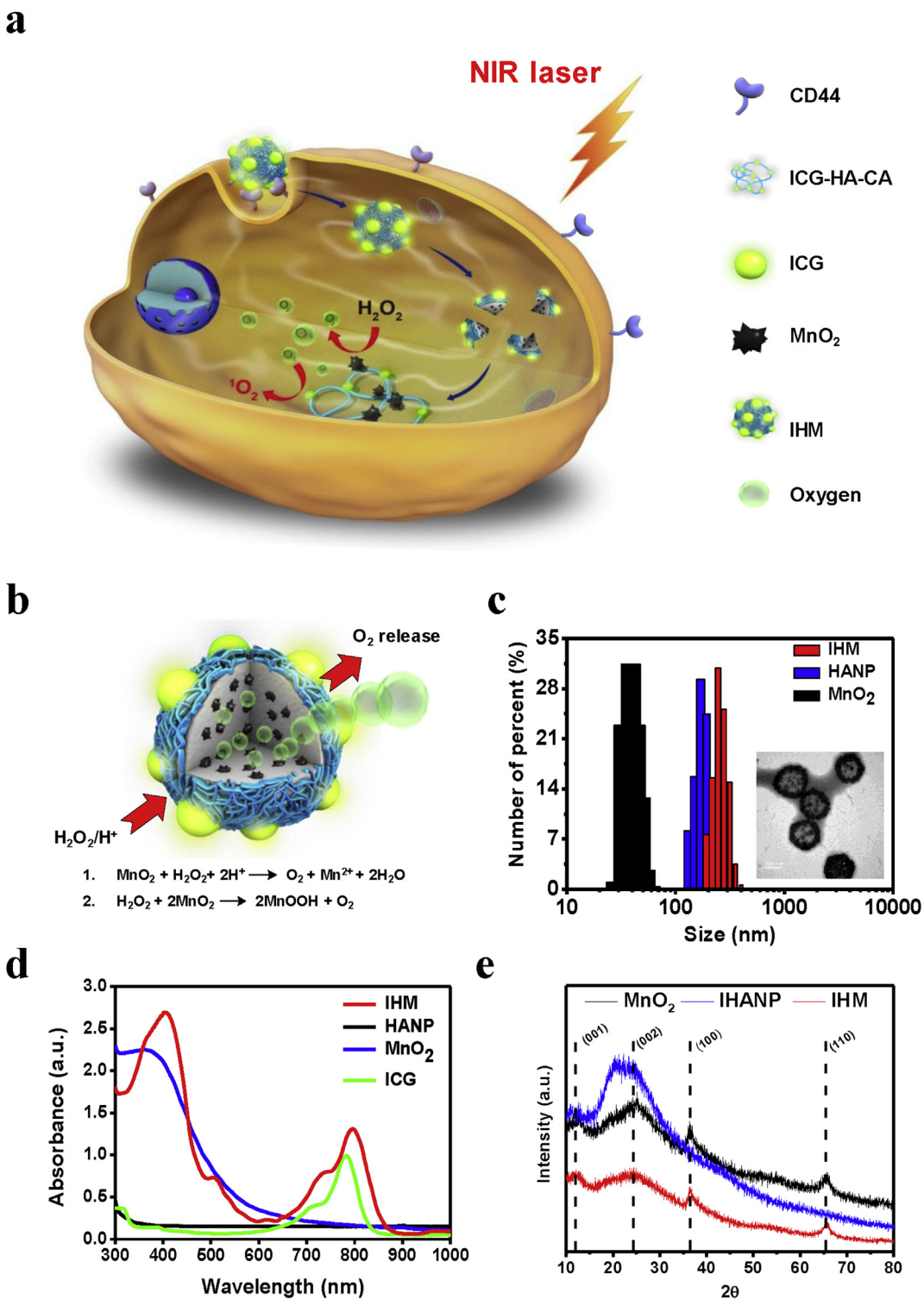

Fig. 1. Preparation and Characterization of IHM. (a) Scheme of IHM for tumor recognition and O_2 evolving for effective PDT under NIR laser illumination. **(b)** Design of IHM. MnO_2 NPs were encapsulated into the reel of thread like HANP with ICG covalently conjugated on the surface. MnO_2 reacted with H_2O_2 and produced rich oxygen for increasing PDT efficiency. **(c)** Dynamic light scattering analysis of HANP (180 ± 4.5 nm), MnO_2 (35 ± 2.5 nm), and IHM (239 ± 5.8 nm). TEM image for IHM is inserted. Scale bar equal to 200 nm. **(d)** UV/vis/NIR absorption spectra of HANP, MnO_2, ICG, and IHM. Characterized peaks of MnO_2 at 400 nm and ICG at 800 nm were observed in IHM, implying the successful construction of IHM. Insert is ICG absorbance spectrum with optimized scale. **(e)** XRD pattern of MnO2, IHANP and IHM. For MnO2 nanospheres, significant XRD peaks were recorded at $2\theta = 12.3$, 24.3, 36.6, and 65.7°, and could be well-assigned to the (001), (002), (100), and (110) planes of MnO2, respectively.

(Fig. S4). Before moving forward, biostability of IHM was identified in water, PBS, FBS, and DMEM. Although MnO_2 precipitated immediately, IHM demonstrated nice dispensability and stability in physiological condition (Fig. S5a). No precipitate and absorbance spectrum changes were found in 48 h (Fig. S5b), supporting that MnO_2 NP was successfully loaded into IHANP. It has to note that the

Table 1
MnO_2 loading efficiency.

Sample (w/w)	Loading contents (%)	Loading efficiency (%)
MnO_2: IHANP (1:9)	6.97	69.7 ± 2.03%
MnO_2: IHANP (1:4)	16.31	81.55 ± 3.31%
MnO_2: IHANP (2:3)	23.54	58.85 ± 4.19%

tumor microenvironment is usually acidic due to the acidic metabolites caused by anaerobic glycolysis in hypoxia. This acidic condition has been considered not only as a key regulator for some lysosomal enzyme activation but also a promoter for certain tumor metastatic factors gene [42,43]. Therefore, the oxygen generation of IHM with H_2O_2 at different pH were tested. As observed by ultrasound imaging in Fig. S6, more amount of oxygen was found when IHM reacts with H_2O_2 at pH 6.5 and pH 7.5, indicating that IHM is more efficient in oxygen generation in acid tumor microenvironment than in neural pH. The same phenomenon was reported elsewhere as well [28]. All of these results illustrated the successful construction of IHM. Compared with the other nanocomplexes for improving the oxygen amount in tumor area [1,27–30], our active/passive tumor targeted IHM provided complementary multi-imaging modalities to guide PDT. As HA is naturally existing in human body, this nanocomplex is less toxic and more promising for clinic translation. Moreover, by changing the surface modification or payload, HANP based nanocomplex can be easily extend to the other theranostic applications.

1.2. Cellular targetability of IHM

Tumor cell targetability was first studied by fluorescent staining on CD44, a cell-surface HA receptor, overexpressed (SCC7), and low (NIH3T3) expressed cell lines [40,44]. It was clear to see that a large amount of IHM bound with SCC7 cells and internalized into the cytoplasm mediated by the overexpressed CD44 on tumor cell surface while free ICG was mostly unbound on SCC7 cells (Fig. S7). To determine IHM specificity to CD44, 100 × excess amount of HANP was added prior to IHM being applied. As expected, little IHM was able to bind to the cells because CD44 was saturated. In addition, when CD44 was expressed low, for example in NIH3T3 cells, the cell labeling efficiency was also found low. Taking these results together, it is considered that IHM has excellent tumor cell targatability and can be internalized into cells efficiently.

1.3. Characterization of oxygen generating and PDT efficiency of IHM

PDT is a new cancer treatment approach that utilize ROS to ablate tumors [45]. Although type I and type II can occur simultaneously [45,46], it has been accepted that type II PDT plays a primary role for the biological PDT effect [6,47]. Therefore, the amount of oxygen in tumors can significantly affect PDT efficacy. Before evaluating the PDT efficacy of IHM, the oxygen generation ability was first studied by an ultrasound imaging system *in vitro*. In our ultrasound images, the white color indicates a strong ultrasound signal, while the black color presents a weak ultrasound signal. When oxygen was produced, tiny bubbles were visualized by ultrasound imaging. H_2O_2 was added exogenously in this *in vitro* study. Because MnO_2 NP is highly reactive with H_2O_2 into Mn^{2+} and O_2, IHM is expected to generate oxygen compared to IHANP without MnO_2 NP. As shown in Fig. 2a, no obvious oxygen bubbles were found in the IHANP group even after H_2O_2 was added. On the contrary, large amounts of oxygen bubbles (white spots) were observed in the IHM group treated with H_2O_2. When more H_2O_2 was added, more oxygen was produced and little oxygen was found without H_2O_2 in the IHM group, suggesting oxygen evolving is H_2O_2 dependent.

To confirm that oxygen evolving is beneficial for SO generation, singlet oxygen sensor green (SOSG) that only responds to SO was utilized in the subsequent study. Strong fluorescent intensity from SOSG (ex/em: 504/525 nm) was observed in the IHM group treated with H_2O_2 after 808 nm laser irradiation (0.3 W/cm^2) over time because of the sufficient oxygen in the system. In contrast, the IHANP group demonstrated a moderate amount of SO and became saturated at about 5 min after laser irradiation due to the quick consumption of oxygen (Fig. 2b). During laser irradiation, a 2.45 ± 0.24 times more amount of SO were detected by SOSG in the IHM group treated with H_2O_2 and laser than that of the IHANP group (Fig. 2c), suggesting that oxygen is helpful in the generation of SO for a successful PDT effect. To further confirm the oxygen producing ability of IHM, the SO generation of IHM in tumor cells was tested subsequently. More oxygen was produced, more SO was formed. First of all, H_2O_2 was gauged in tumor cells by a commercial 2′,7′–dichlorofluorescin diacetate (DCFDA) kit [8,20,48].

As Fig. S8 shows, non-fluorescent DCFDA was deacetylated and oxidized into fluorescent 2′,7′–dichlorofluorescein (DCF, ex/em: 495/529 nm) in SCC7 cells by intracellular H_2O_2\ and visualized by fluorescent microscopy, suggesting the amount of H_2O_2 is sufficient in tumor cells. Next, SCC7 cells were treated with IHM and irradiated with the NIR laser. The generation of SO intracellular of SCC7 was stained by SOSG and visualized in fluorescent microscopy. Strong fluorescent signals were observed in the IHM-treated cells after laser irradiation, while weak signals were found in the IHANP-treated group. No fluorescent signals were detected in the free SOSG-treated group and SO inhibitor-treated group, implying that the fluorescent changes were caused by reactions between SO and SOSG specifically. It is important to note that H_2O_2 was not visualized by SOSG. Given the importance of oxygen in cancer PDT, it is considered that IHM-treated cells will generate more oxygen and in turn produce more SO under laser irradiation.

1.4. Cytotoxicity study with IHM

In light of the outstanding SO generation ability and tumor targetability, cytotoxicity of IHM was evaluated in SCC7 cells using the Cell Counting Kit-8 (Sigma-Aldrich, MO, USA). In the IHM system, ICG, which has already been approved by the U.S. FDA for clinical applications and it was reported as a photosensitizer with NIR absorbance, was helpful for deep tissue penetration. Hyaluronic acid is a naturally existing reagent in the human body and has been widely used in cosmetics. In addition, after reacting with H_2O_2 in the tumor to produce oxygen for improving PDT efficacy, MnO_2 decomposed into non-toxic and soluble Mn^{2+} ions. Thus, it is expected that without NIR laser activation, toxicity of IHM is negligible. The tumor cell ablation effect will mostly depend on the IHM mediated PDT. As shown in Fig. 3a, little toxicity of both IHM and IHANP was detected without laser illuminated. When an 808 nm laser was applied (0.5 W/cm^2, 10 min), a significant SCC7 cell proliferation was observed suppressed in IHM- and IHANP-treated groups induced by PDT; however, more cells (86.83± 4.13%) were found dead in the IHM group in which production of more SO than the IHANP group was found (56.88± 8.60%) (Fig. 3). To verify advantages of IHM over IHANP, the effect of tumor cell ablation was compared among different materials by calcein-AM and propidium iodide (PI) staining. As shown in Fig. 3b, almost all cells were dead after the IHM treatment while more cells survived in the IHANPT-treated group. No toxicity was observed for MnO_2- and ICG-treated cells without laser irradiation. The strong tumor cell proliferation ablation property of IHM-mediated PDT demonstrated

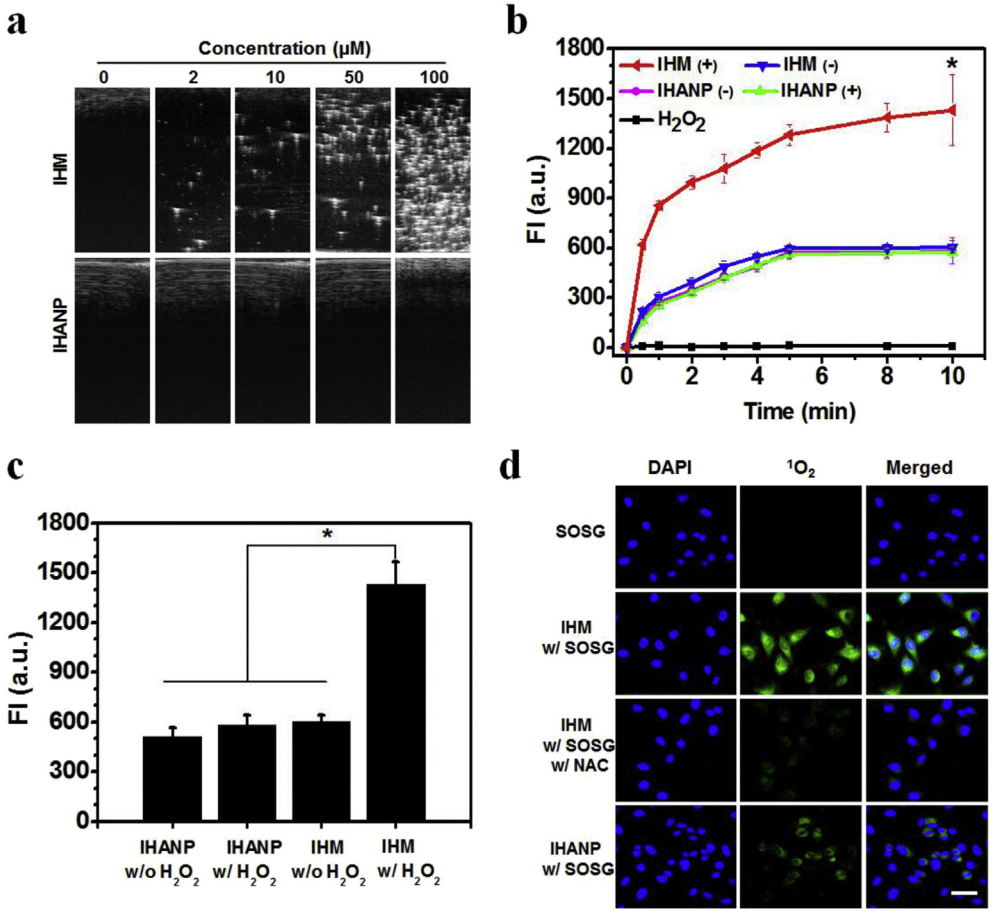

Fig. 2. Enhanced $^1O_2$ generation of IHM *in vitro* and intracellular. **(a)** Ultrasound images observed the O_2 generation of IHM in different amounts of H_2O_2 (0, 2, 10, 50 and 100 μM). No O_2 was detected in the IHNAP with H_2O_2 group. The white color was set as the high ultrasound signal and black color was considered as the low ultrasound signal. **(b)** *In vitro* $^1O_2$ generation of IHANP and IHM with (+) and without (−) H_2O_2 under NIR laser irradiation (808 nm laser, 0.15 W/cm^2) for a continuous time. *P < 0.05. A time dependent ROS generation of IHANP and IHM was observed. In the presence of H_2O_2, IHM generated more ROS after being irradiated by the NIR laser. **(c)** *In vitro* $^1O_2$ (SO) generation of ICG, IHANP, and IHM with H_2O_2 under NIR laser irradiation (808 nm laser, light dose rate: 0.3 W/cm^2). *P < 0.05. Because of the O_2 evolving ability, IHM was able to generate the most amount of ROS. **(d)** Detection of SO generated by IHM in SCC7 cells. More SO was observed in IHM-treated cells, while less SO was found in IHANP-treated cells in the existence of laser irradiation. The generation of SO can be inhibited by NAC, a ROS scaavenger, even with laser illumination. Scale bar equals to 50 μm.

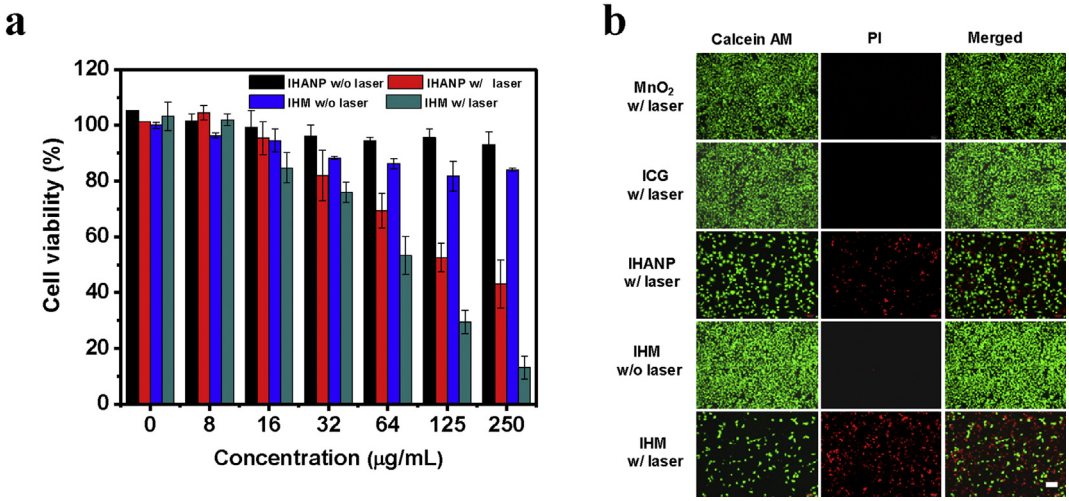

Fig. 3. Enhanced cytotoxicity of IHM after laser irradiation. **(a)** Relative viabilities of SCC7 cells after incubation with IHANP and IHM at different concentration with or without 808 nm laser irradiation (0.5 W/cm^2, 10 min). Those cells were then washed with PBS and incubated in fresh cell medium for 24 h before MTT assay was conducted. **(b)** Calcein AM/PI staining to visualize SCC7 cell viability treated with MnO_2, ICG, IHANP, and IHM (with or without laser irradiation). Green color is Calcein AM (ex/em = 490/515 nm) showing staining of live cells and the red color is propidium iodide (PI; ex/em = 535/615 nm) showing staining of dead cells. Values are means ± SD (n = 3). Scale bar equals to 100 μm. (For interpretation of the references to colour in this figure legend, the reader is referred to the web version of this article.)

that IHM can inhibit SCC7 cell proliferation in a dose-dependent manner more efficiently compared with IHANP and ICG with the same laser irradiation.

1.5. Tumor accumulation and biodistribution of IHM in the tumor-bearing mouse model

Encouraged by the remarkable tumor targetability and oxygen evolving facilitated PDT effect *in vitro*, tumor accumulation and biodistribution of IHM was studied *in vivo*. One hundred μL of IHM (360 μg of IHM, equivalent to 58 μg of MnO_2 or 20 μg of ICG) was intravenously (i.v.) injected into the SCC7 tumor-bearing mouse model and fluorescent images were taken at indicated time points post-injection (p.i.). Free ICG (20 μg) was also i.v. administrated as a control. Excitation and emission wavelengths were set for ICG as 780/800 nm (Fig. S3). As shown in Fig. 4 a and d, strong fluorescent signals were observed in the IHM-administered group in a time dependent manner. The tumor-to-muscle (T/M) ratio at 1, 4, 6, 12, and 24 h p.i. was calculated as 1.15 ± 0.22, 2.03 ± 0.31, 4.03 ± 0.36, 2.61 ± 0.30, and 1.87 ± 0.24 respectively, indicating IHM would accumulate mostly in the tumor at 6 p.i. No significant fluorescent signals were observed gathering at the tumor site in the ICG-injected group due to the lack of targetability. To confirm the tumor accumulation and specificity of IHM, SCC7 tumor-bearing mice received IHM were sacrificed at 6 h p.i. and major organs were excised and collected for fluorescent imaging. As shown in Fig. S9, fluorescent intensity was found highest in the tumor than the other normal organs including the heart, kidneys, liver, lung muscle, and spleen. It is not a surprise that some IHM accumulation was found in the liver due to the uptake of phagocytic cells in the reticulo-endothelial system and by the liver sinusoidal endothelial cells expressing another HA receptor (HARE) as we and others observed before [20,49], which can be significantly optimized by modification of more hydrophilic reagents, for example poly(ethylene glycol) (PEG) [44].

In addition to fluorescent imaging, photoacoustic (PA) imaging is another new imaging modality with high resolution and deep imaging depth. Compared to whole body fluorescent imaging, although PA imaging can only image a region of interest, it is able to provide a detailed bioinformation, for example blood vessel distribution and imaging agents accumulating in the tumor. Due to the strong photoacoustic effect of ICG (Fig. S4), PA imaging was applied to analyze the tumor accumulation of IHM. As shown in Fig. 4 b and e, IHM accumulation was clearly observed in tumor blood vessels over time. Compared to the signals before IHM was injected, PA signals in the tumor were found increase by 1.45 ± 0.24, 1.9 ± 0.35, 3.58 ± 0.29, 2.93 ± 0.13, and 2.13 ± 0.28 times at 1, 4, 6, 12, and 24 h p.i., respectively (Fig. 4e). This accumulation also peaked at 6 h p.i. as fluorescent imaging demonstrated and started to decrease after 6 h p.i. A similar biodistribution of IHM was observed by PA imaging *ex vivo* as fluorescent imaging, confirming that IHM holds excellent tumor targetability and specificity (Fig. S10). These imaging results verified that IHM can accumulate in the tumor effectively and the 6 h p.i. time point is the most appropriate to initiate PDT because of the maximum accumulation of IHM in the tumor.

Besides the excellent tumor targeting, we also evaluated the IHM oxygen generating potency in tumor by ultrasound imaging. As shown in Fig. 4c, after systematic administration, oxygen was observed increasing in the tumor over time in the IHM-injected SCC7 tumor, while the oxygen amount was not found to change significantly in ICG-treated mice. Echo intensity in the tumor was quantified to represent the amount of oxygen and the most oxygen was detected at 6 h p.i. when IHM peaked as confirmed by fluorescent and photoacoustic imaging. It has been reported that tumor

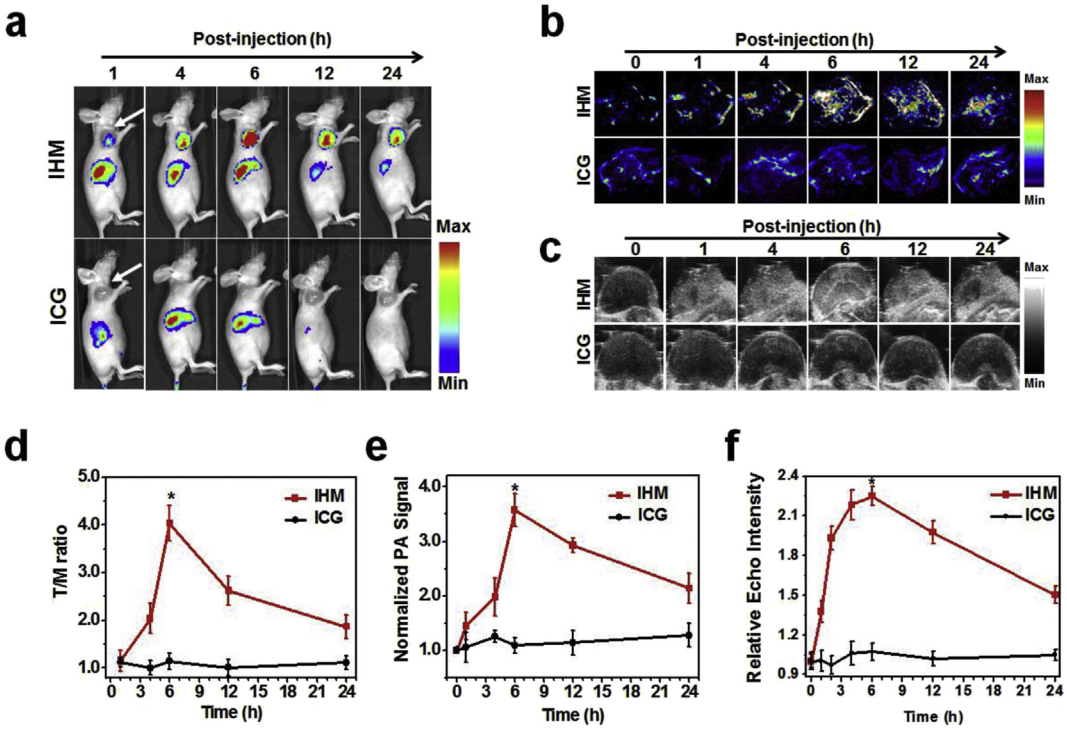

Fig. 4. Non-invasive *in vivo* imaging monitoring the tumor accumulations of IHM. **(a)** NIR fluorescent imaging of intravenously injected IHM accumulation in SCC7 tumor-bearing mice at different times. Arrows indicate the tumors location. **(b)** Photoacoustic imaging of intravenously injected IHM accumulation in SCC7 tumor-bearing mice at different times. **(c)** Ultrasound imaging monitoring the generation of O_2 in tumors after intravenously injected IHM. **(d)** Tumor/muscle (T/M) ratio of SCC7 tumor-bearing mice administered IHM and ICG, suggesting IHM peaked in tumor at 6 h p.i. **(e)** Normalized PA signals of SCC7 tumor-bearing mice administered IHM and ICG, suggesting IHM peaked in tumor at 6 h p.i. **(f)** Relative echo intensity of SCC7 tumor-bearing mice administered IHM and ICG, suggesting the O_2 amount peaked at 6 h p.i.

cells are able to generate large amount of H_2O_2 at a constant rate, which will be on a log scale when cell numbers are increased over to a certain amount [32]. Thus, the IHM reaction with H_2O_2 is on a slow and time-dependent manner, which is also consistent with the other reports [27,28,50]. Compared to the oxygen amount before injection, oxygen in the IHM-treated tumor was found to increase by 2.25 ± 0.07 fold. However, oxygen changes were not detectable in the ICG and IHANP-administered groups (Fig. 4 and S11). Because the near-infrared (NIR) optical absorbance peak of hemoglobin would change from its deoxygenated status (750 nm) to the oxygenated state (850 nm), the absorbance of hemoglobin at 750 and 850 nm are commonly adopted for PA imaging to evaluate the blood oxygenation status as reported [30]. We measured oxygen changes before and after IHM injection (Fig. S12). More oxygen was detected by PA imaging in HANP/MnO_2 group than control groups. It has to note that we did not use IHM to confirm the oxygen generation here as ICG will affect the PA signal with hemoglobin. Therefore, we further confirmed that the 6 h time point was suitable for PDT due to maximum oxygen being produced by IHM in the tumor, and this significantly improved PDT's therapeutic effect.

1.6. In vivo PDT by systematic administration

At last, PDT efficiency of IHM was evaluated by monitoring tumor ablation. When tumor volume reached around 80 mm^3, SCC7 tumor-bearing mice were randomly divided into eight groups (n = 5/group): mice treated with HANP without (w/o) laser irradiation, mice treated with HANP with (w/) laser irradiation, mice treated with ICG without laser irradiation, mice treated with ICG with laser irradiation, mice treated with IHANP without laser irradiation, mice treated with IHANP with laser irradiation, mice treated with IHM without laser irradiation, and mice treated with IHM with laser irradiation. To achieve a therapeutic effect, HANP, ICG, IHANP (287 μg of IHANP, equivalent to 20 μg of ICG), and IHM (360 μg IHM, equivalent to 58 μg of MnO_2 or 20 μg of ICG) were injected intravenously into tumor-bearing mice, respectively. At 6 h p.i. when IHM peaked in the tumor and maximum oxygen was produced, an 808 nm (0.8 W/cm^2, 10 min) laser was applied to tumors to initiate PDT. Since ICG was also known as a photothermal therapy agent [20], an IR thermal camera was used to monitor and control the tumor temperature below 42 °C in all groups. The tumor sizes were recorded every other day to verify the PDT effect for up to 14 days (Fig. 5). Although the IHANP-treated tumor was indeed ablated in the first 6 days after PDT, it started to grow after that time, implying that the low power laser irradiation cannot fully inhibit the tumor growth due to the low oxygen-induced insufficient PDT. In a marked contrast, tumors in the IHM-treated group were ablated significantly and cured after 14 days (Fig. 5a). No recurrence was observed in 30 days and most mice survived (Fig. 5b), suggesting that oxygen-generating IHM attenuated the low PDT efficiency in the tumors. A slight ablation was noticed in the ICG-administered tumors due to the non-targetability and low tumor uptake of ICG. Tumor growth rate was not obviously affected in the rest of the groups and most of the mice died due to the extremely large tumor (Fig. 5c). At end of our study, 80% mice with IHM treated survived because one mouse with sever proctoptosis was requested to be sacrificed. As most proctoptosis occurred in nude mouse is due to the immunodeficiency, we consider IHM did not have a bad affect on this sacrificed mouse. Mice body weight were not found to change for all groups (Fig. 5d).

To study the *in vivo* toxicity of IHM, tumor tissues and normal organs were harvested and subjected to H&E staining. Nuclear will be stained as dark blue and cytoplasm will be stained as pink. As shown in Fig. S13, severe tumor tissue damage was clearly observed in the IHM-treated tumor compared with tumors in other groups, suggesting that PDT was effective and efficient because of the abundant oxygen in IHM-treated tumor during PDT. Typical dead cells stained by H&E was labeled by red arrows in IHM groups and there are little live cells with intact cytoplasm. On the contrary, the tumor tissue structure was less damaged in IHANP group due to the less efficient PDT compared with IHM treated group. No destruction was found in normal organs with or without laser irradiation, consistent with the unaffected body weight. These results demonstrated that because of the sufficient intratumoral oxygen evolving property, IHM is an effective PDT agent for tumor ablation with negligible side effects.

In order to account for the significant improvement of tumor PDT, several factors were taken into consideration. First, caspase-3, the apoptosis initiator, was evaluated in IHM-, IHANP-, and HANP-treated tumors after laser irradiation because one of the possible pathways of the PDT ablate tumor is inducing tumor cells apoptosis [8]. It can be seen in Fig. 6 that an elevated caspase-3 expression was detected in the IHM tumors with laser irradiation, while quite a bit of caspase-3 was seen in the IHANP-treated tumors even with laser irradiation. Little caspase-3 was found in the HANP-treated tumors after laser irradiation, suggesting that PDT in the IHM-treated tumors are more effective in tumor ablation. Little capase-3 elevation was detected compared to the IHM-treated group (Fig. S14). Afterwards, two hypoxia markers, pimonidazole and hypoxia-inducible factor 1-α (HIF1-α), were analyzed. As expected, little pimonidazole and HIF1- α were observed in the IHM-treated tumor with laser irradiation due to the oxygen-evolving attenuated tumor microenvironment (Fig. 6). In contrast, IHANP- and HANP-treated tumors were found to have a high expression of pimonidazole and HIF1-α, due to the hypoxia pre-existing condition and consumption of oxygen in the tumor (Figs. S15 and S16). Collectively, the expression changes of biomarkers demonstrated that IHM can effectively ablate the tumor by inducing apoptosis via efficient PDT. The generation of oxygen not only attenuated tumor hypoxic microenvironments, but also improved tumor treatment efficiency. Overall, these results confirmed that IHM can significantly improve PDT effect by producing sufficient oxygen in the tumor which facilitated tumor ablation.

2. Conclusion

In this work, we successfully designed a novel oxygen-generating agent, IHM, to improve PDT efficacy by encapsulation of MnO_2 NP into IHANP nanoparticles. The encapsulated MnO_2 can sensitively react with the unnecessary metabolic H_2O_2 in the tumor to produce oxygen molecules after IHM was broken up by hyaluronidase in tumor cells. Abundant oxygen was detected *in vitro* and *in vivo* by ultrasonic imaging. With the guide of fluorescent and photoacoustic imaging, the oxygen-generating IHM-treated group ablated tumor growth with PDT more effectively than the IHANP-treated tumors, which were not able to provide oxygen inside tumors. Immunofluorescent staining confirmed both HIF1- α and pimonidazole decreased in the IHM-treated group, implying the oxygen generating in the tumor not only improves PDT efficacy, but also attenuates tumor hypoxia. Additionally, no obvious toxicity of IHM was found in the IHM-treated mouse organs by H&E examination. When these results are taken together, it is considered that IHM holds great potency for fluorescent and photoacoustic imaging-guided tumor PDT with remarkably improved efficacy, especially for those hypoxia tumors. Overall, our design of IHM can be an alternative way for imaging-guided enhanced tumor PDT with oxygen-generating capability. More importantly, the IHM attenuated hypoxia environment can also be beneficial for chemotherapy and radiation therapy. Related work is under investigation in our group.

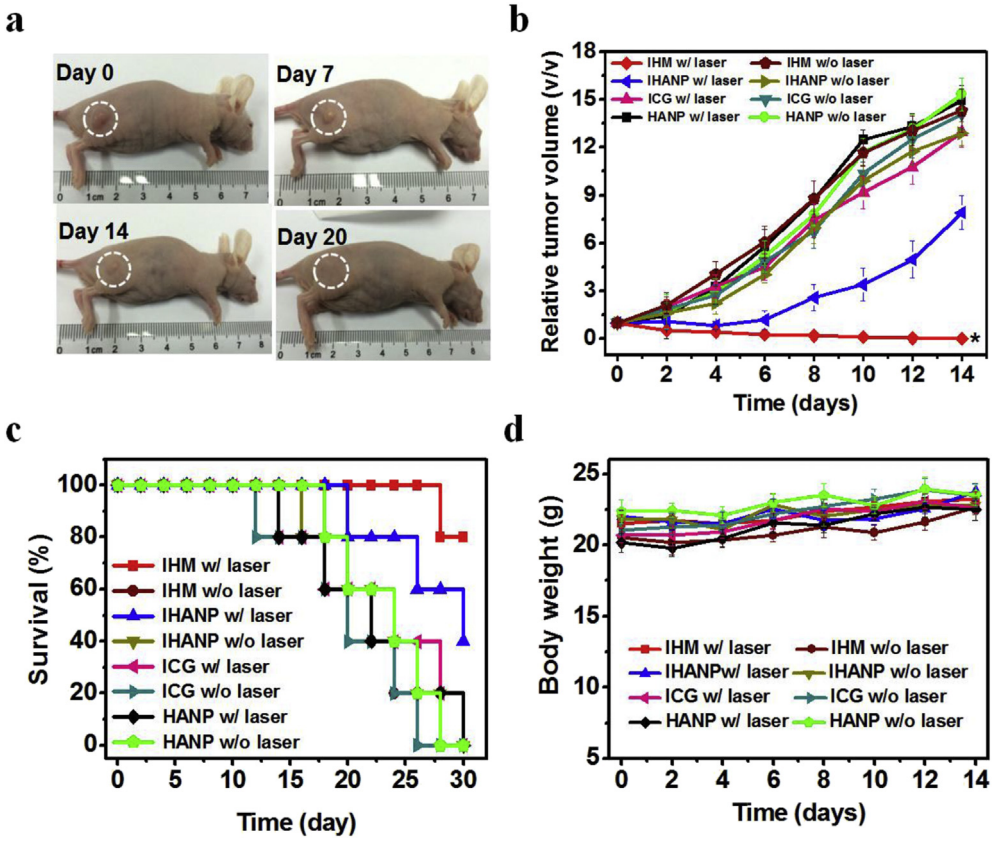

Fig. 5. ***In vivo*** **PDT effect of IHM by intravenous administration into a SCC7 tumor mouse model. (a)** Typical photographs of SCC7 tumor-bearing mice at different days after IHM treatment. **(b)** Tumor growth curves of different groups of SCC7 tumor-bearing mice. Error bars represent the standard deviations of 5 mice per group. *P < 0.05. **(c)** SCC7 tumor-bearing mice survival rate after receiving different treatments. **(d)** Body weight of the mice was measured during the 14-day evaluation period under the different conditions.

3. Materials and methods

3.1. Reagents

Sodium hyaluronic acid (HA, 234 kDa) was bought from Lifecore Biomedical Company (MN, USA). Ethylenediamine (EDA), 1-ethyl-3(3-(dimethylamino)propyl)carbodiimide (EDC), and N-hydroxysuccinimide (NHS) were obtained from J&K Company (Beijing, China). 5β-Cholanic acid (CA), tetrabutylammonium hydroxide (TBA), and propidium iodide (PI) were purchased from Sigma-Aldrich Co. (MO, USA). Amine-PEG-amine (molecular weight = 2 kDa) was purchased from Shanghai Seebio Biotechnology (Shanghai, China). ICG-Sulfo-Osu (ICG) was obtained from Dojindo Molecular Technologies (Tokyo, Japan). A CCK-8 assay kit and 4,6-diamidino-2-phenylindole (DAPI) were purchased from Sangon Biotech Co. (Shanghai, China). Calcein-AM was obtained by Invitrogen (NY, USA). SCC7 (squamous cell carcinoma) was bought from American Type Tissue Culture Collection (ATCC) (VA, USA). The 2′,7′-dichlorofluorescenindiacetate (DCFDA) and singlet oxygen sensor green (SOSG) kit were purchased from Thermo Fisher Scientific (MA, USA). Caspase-3 antibody was purchased from Abcam (MA, USA). FITC conjugated goat anti-rabbit immunoglobulin G was obtained from Life Technologies (NY, USA).

3.2. Preparation of IHANP

The following HANP conjugations were performed according to the previously described procedures with slight modifications [20,40]. Briefly, amine-PEG-amine (NH_2-PEG-NH_2) and free ICG were dissolved in anhydrous DMSO containing 3% of DIPEA and stirred for 40 min at room temperature. The synthetic NH_2-PEG-ICG was then purified by HPLC using a linear gradient of 10%–65% acetonitrile/water (0.1% TFA) for 30 min at 3.5 mL/min and then lyophilized. Meanwhile, to dissolve hyaluronic acid (HA) in anhydrous DMSO, HA was converted to the tetrabutylammonium salt of HA (HA-TBA) according to previously reported methods [40]. The HA-TBA was then chemically modified with 5β-cholanic acid (CA) in the presence of EDC and NHS at 60 °C. After 40 min, NH_2-PEG-ICG was then added into the reaction solution and stirred overnight at room temperature. The reaction solution was dialyzed against methanol/ultrapure water (1:1, v/v) and ultrapure water for 4–12 h. After being lyophilized, HA-CA-ICG (IHANP) was obtained and stored at 4 °C in the dark until further use.

3.3. Preparation of MnO_2 nanoparticle (MnO_2 NP)

MnO_2 was prepared according to the literature [39]. Briefly, 0.25 g of $KMnO_4$ was dissolved in 125 mL of distilled water, and the mixture was stirred for about 0.5 h. A total of 2.5 mL of oleic acid was added, and a steady emulsion was formed. After the emulsion was maintained at room temperature for 24 h, a brown-black product was collected, and washed several times with distilled water and alcohol to remove any possible residual reactants. Finally, the product was dried in air at 60 °C for 12 h.

3.4. Preparation of IHM

IHANP loaded with MnO_2 (IHM) was readily prepared by mixing

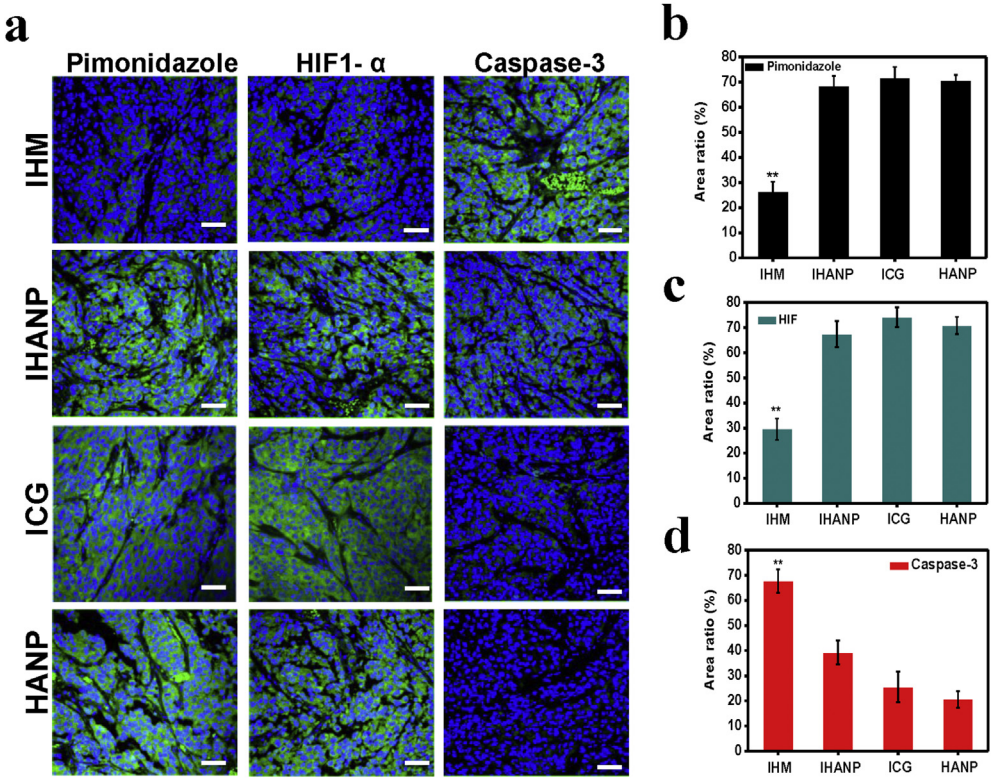

Fig. 6. Effect of IHM on tumor hypoxia and tumor ablation. (a) Representative images of tumors treated with IHM, IHANP, and HANP after laser irradiation. Hypoxic section was visualized by pimonidazole and HIF1-α staining. An attenuated hypoxia was observed in the IHM-treated tumors after laser irradiation, while severe hypoxia was confirmed in the IHANP- and HANP-treated tumors with laser illumination. PDT-induced tumor apoptosis was detected by the caspase-3 antibody. Due to sufficient oxygen in tumors after IHM treatment, a large amount of caspase-3 expression was found, suggesting PDT induced apoptosis effectively. Low expression of caspase-3 was detected in the IHANP-treated group. Little caspase-3 was observed in the HANP-treated group. Scale bar equal to 20 μm. (b) Quantification of pimonidazole, HIF-α and caspase-3 expression.

MnO_2 dissolved in trichloromethane with IHANP in ultrapure wat and homogenized (D-3L, PhD Technology LLC, MN, USA) for 15–20 min (20 000–25 000 psi). The resulting mixture was added into the ultrafiltration tube (Cut off = 100 kDa) and was further centrifuged at 8000 rpm for 30 min to remove free MnO_2, then freeze dried.

3.5. Characterization of IHM

The particle size and size distribution of IHM NPs were measured by dynamic light scattering DLS (Varian Medical Systems, Palo Alto, USA). Zeta potential measurements were performed at 25 °C on a Malvern Zeta Size-Nano Z instrument (UK). The nanostructure and size of IHM were observed by transmission electron microscopy (TEM) (Bruker, Germany). UV–vis absorbance spectra of HANP, MnO_2, ICG, and IHM were observed with the Multiskan GO microplate reader (Thermo Fisher Scientific, MA, USA). Fluorescent signals of ICG and IHM were measured using a fluorescence spectrophotometer (Varian Medical Systems, Palo Alto, USA). X-ray diffraction (XRD) patterns of the samples were analyzed by a Rigaku Ultima IV X-ray diffractometer equipped with a Cu radiation source using an operation voltage and current of 40 kV and 40 mA.

3.6. In vitro photoacoustic tomography

IHM and ICG contained the same amount of ICG (16, 8, 4, 2, and 1 μg/mL), IHM and MnO_2, which contain the same amount of MnO_2, were subjected to PA imaging. HANP, MnO_2, ICG, and IHM were put into Eppendorf tubes (1.5 mL) before imaging and all the tubes were immersed at the same depth in the deionized water. Photoacoustic tomography of all samples were captured at 808 nm using Endra Life Sciences's Nexus128 (MI, USA).

3.7. In vitro ultrasonography of O_2 bubbles from IHM

An ultrasound imaging system (Toshiba Nemio 30, Japan) was utilized to visualize the O_2 bubbles generated by IHM NPs in a test tube containing H_2O_2 at different concentrations. As the IHM and IHANP were respectively injected to H_2O_2, the contrast was monitored by the Vevo 770 micro-US imaging system (VisualSonics, Ontario, Canada, RMV-704, 40 MHz, B-mode).

3.8. In vitro enhanced $^1O_2$ generation of IHM

A commercial $^1O_2$ kit, singlet oxygen sensor green (SOSG), was employed to study IHM enhanced generation of $^1O_2$. The fluorescence of SOSG is quenched in its intact form and produces strong fluorescence after $^1O_2$ oxidation. To verify the potentiated $^1O_2$ generation potency, aqueous solutions of IHANP and IHM were added into 1.5 mL Eppendorf tubes containing SOSG solution. Then in the experimental groups, 10 μM of H_2O_2 ultrapure water solution was added and an 808 nm continuous laser was applied at a power of 0.3 W/cm^2 for 10 min. The entire surface of the samples was adjusted to confirm that they were covered by the laser spot. The fluorescent intensity that is proportional to the amount of $^1O_2$ was measured every minute and detected with the fluorescence spectrometer with 490 nm excitation and 525 nm emission. The control groups were incubated under the same conditions without H_2O_2.

3.9. Cell culture and cell internalization of HANP

Human squamous cell carcinoma cell line (SCC-7 cells) and NIH-3T3 cells were cultured in an 8-well chamber in Dulbecco's Modified Eagle Medium (DMEM)/high glucose medium supplemented with 10% FBS and 1% antibiotic solution at 37 °C and 5% CO_2. The next day both cells were washed by cold PBS and incubated with IHM (280 μg/mL containing 20 nM ICG) at 37 °C for 4 h with 5% CO_2 atmosphere. For the blocking test, free HANP (1 mg/mL) was added to cells 30 min before IHM was applied. After incubation, all cells were washed by cold PBS thoroughly. The cells were finally fixed in cold ethanol for 15 min at −20 °C and cells were mounted with medium containing DAPI for 10 min in the dark. Cell targetability of IHM was observed by a confocal microscope (Leica Microsystems, Germany) and the excitation and emission wavelengths were set at 780 nm and 800 nm for ICG, respectively.

3.10. Confocal fluorescence imaging

We assessed the intracellular H_2O_2 levels with 2′,7′- dichlorofluoresceindiacetate (DCFDA), a H_2O_2 indicator that can be rapidly oxidized by H_2O_2 to emit green fluorescence. Human squamous cell carcinoma cell line were maintained following protocols provided by the American Type Tissue Culture Collection. One day before imaging, cells were passed and plated on 18 mm glass bottom dishes. The next day, both cells were washed by cold PBS and incubated with DCFH at 37 °C for 6 h with 5% CO_2 atmosphere. Cells in control groups were pretreated with N-acetylcysteine (NAC) as a ROS scavenger. At last, cell imaging was carried out after washing cells with PBS three times. Confocal fluorescence imaging studies were performed with a confocal microscope (Leica Microsystems, Germany).

Further, a singlet oxygen sensor green (SOSG) reagent was employed to study IHM enhanced generation of $^1O_2$. One day before imaging, cells were passed and plated on 18 mm glass bottom dishes. The next day, both cells were washed by cold PBS and incubated with both IHM and 2 μL SOSG working solution at 37 °C for 6 h with 5% CO_2 atmosphere. Cells in the control groups were pretreated with N-acetylcysteine (NAC) as a ROS scavenger. Then the groups were exposed to 808 nm laser (0.5 W/cm^2) irradiation for 5 min. Lastly, cell imaging was carried out with a confocal microscope (Leica Microsystems, Germany) after washing cells with PBS for three times.

3.11. Cytotoxicity

The SCC7 cells were seeded in a 96-well plate at a density of 8000 cells per well, and cultured overnight at 37 °C in a 5% CO_2 incubator. The next day, cells were washed with PBS and incubated with IHANP and IHM solutions at a series of concentrations for 6 h under the same condition (the ICG content in this HANP formulation were measured to be 6.6%). After being washed with PBS, the experimental cell medium was replaced with fresh DMEM culture medium (100 μL) and exposed to the 808 nm laser for 10 min (0.5 W/cm^2). Subsequently, cells were placed at 37 °C in a 5% CO_2 incubator for 12 h. The other groups were incubated under the same conditions without irradiation. Cell viability was evaluated by the CCK-8 assay kit. The optical density (OD) was measured at 450 nm and recorded by a microplate reader.

Enhanced photodynamic therapy was also investigated by 3′6′-Di (Oacetyl) -4′5'-bis [N, N-bis (carboxymethyl) aminomethyl] fluorescein, tetraacetoxymethyl ester (Calcein AM)/Propidium Iodide (PI) staining (Sangon Biotech, Shanghai, China). The SCC7 cells were seeded in a 6-well plate with a density of 1×10^5 cells and grown to 80–90% confluence. The SCC7 cells were incubated with parallel concentrations of HANP, free ICG, IHANP, and IHM for 6 h. After being washed with PBS several times and immersed in fresh culture medium (1 mL), the experimental groups were imaged with the laser beam (808 nm, 0.5 W/cm^2) for 10 min followed by incubation for 12 h at 37 °C and 5% CO_2. Control groups in the dark were incubated in fresh DMEM medium. After removing fresh DMEM medium, calcein AM (4 μmol/L) and PI solutions (4 μmol/L) in PBS were added to SCC7 cells and incubated for 30 min at 37 °C with 5% CO_2. Finally, PBS was used to clean the cells three times. Images of the cells were obtained by fluorescence microscope.

3.12. In vivo FL and PA imaging of SCC7 tumor xenografts in nude mice

Animal experiments were conducted under protocols approved by Animal Care and Use Committee (CC/ACUCC) of Xiamen University. Subcutaneous sites of athymic nude mice (seven weeks old, female, 20–24 g) were injected with a suspension of 4×10^6 SCC7 cells in PBS (80 mL). When the tumor size (in the right leg region) reached average size of 80 mm^3, mice were randomly allocated into two groups: (a) IHM (360 μg of IHM containing 58 μg of MnO_2 and 20 μg of ICG) were injected into the tail vein of the mice and (b) free ICG (20 μg) were injected into the tail vein of the mice. Fluorescent images were acquired at 1, 4, 6, 12, and 24 h after injection using IVIS Lumina II (Caliper Life Sciences, MA, USA; Excitation Filter: 740 nm, Emission MFilter: 780 nm).

When tumor volumes reached 80–100 mm^3, mice were randomly allocated into two groups: IHM ((360 μg of IHM containing 58 μg of MnO_2 and 20 μg of ICG) and free ICG (20 μg) were injected into the tail vein of the tumor-bearing mice. After injection, PA images of the tumor sites were recorded on Endra Life Science's Nexus128 (808 nm) at 0, 1, 4, 6, 12, and 24 h. At 6 h after the one-dose injection, SCC7 tumors and normal organs (the heart, liver, spleen, kidneys, pancreas, and muscle) were collected for acquisition of photoacoustic signal.

3.13. In vivo ultrasound (US) imaging

The tumor-bearing mice were anesthetized using 2% isoflurane (Abbott Laboratories, IL, USA) mixed with 100% O_2 delivered using a veterinary anesthesia delivery system (ADS 1000; Engler Engineering Corp., FL, USA). For the echo images of O_2 produced from IHM, IHM (360 μg of IHM containing 58 μg of MnO_2 and 20 μg of ICG) was injected via the tail vein. The images were obtained by a Vevo 2100 micro-US imaging system (Visual Sonics MS-250D, 40 MHz, B-mode) on pre-injection, immediately after post-injection, and in the course of 1, 2, 4, 6, 12, and 24 h of US irradiation.

In order to investigate the change of oxygen content at the tumor site before and after PDT treatment, the other dose was administrated following the same procedure. The tumors were exposed to 808 nm laser irradiation for 10 min at 6 h post-injection. The echo images were obtained pre-irradiation and immediately post-irradiation. The signal intensities of echo imaging were measured using Vevo 2100 Workstation Software.

3.14. In vivo photodynamic therapy

SCC7 cells (4×10^6 cells in 80 μL of PBS) were injected into the right leg of athymic nude mice (seven weeks old, 20–24 g). When the tumor size reached 80–100 mm^3, SCC7 tumor-bearing mice were randomly divided into 8 groups: (a) IHM without laser, (b) IHM with laser, (c) IHANP without laser, (d) IHANP with laser, (e) free ICG without laser, (f) free ICG with laser, (g) HANP without laser and (h) HANP with laser. Tumor volumes were determined

using the formula: $V = a \times (b^2)/2$, where a is the length and b is width of each tumor in mm respectively. Compared to the original tumor volume, the volume of the tumor was evaluated by normalizing the measured values. 100 μL of IHM at concentration of 3.6 mg/mL (360 μg of IHM containing 58 μg of MnO_2 and 20 μg of ICG), IHANP (287 μg of IHANP, equivalent to 20 μg of ICG), free ICG (20 μg), and HANP were injected into the tail vein of the SCC7 tumor-bearing mice, respectively. All groups were received only one inject for PDT treatment. At 6 h post-injection, tumors were irradiated with the 808 nm laser at a power density of 0.8 W/cm^2 for 10 min. In order to verify the potentiated PDT efficiency of IHM, thermal images in tumors were taken using a FLIR A5 camera and all groups received interrupted laser to maintain a constant temperature (42 °C) to avoid photothermal effect.

Relative tumor volumes of all groups were calculated for 14 days after the treatment. The body weight of the mice was measured at the same time points. After 14 days of treatment, the relative tumor volumes of all groups were calculated. Animals were killed and tumors and major organs were collected for analysis. For the IHM-treated group, tumors were collected on Day 3 after laser irradiation. Histological changes and apoptotic cells in tumor tissues and main organs were evaluated using hematoxylin and eosin (H&E) staining.

3.15. Fluorescent immunostaining

The tumors were dissected and sliced by frozen section procedure into 10 μm sections at predetermined time points. To observe PDT induced apoptosis at the tumor site, the Caspase-3 antibody was applied to stain on the tumor tissues from the diverse treated groups. For the detection of hypoxia in the tumor, the hypoxia marker, pimonidazole, was stained by a commercial Hypoxyprobe-1 plus kit (Hypoxyprobe, Inc., USA) following the protocol provided. Polyclonal rabbit anti-HIF-1α antibody (dilution 1:100, Novus Biologicals) was used to detect the expression of HIF-1α as the primary antibody. After washing, the primary antibody was detected by sequential application with FITC conjugated goat anti-rabbit immunoglobulin G. Cell nuclei were visualized with DAPI and slides were imaged with a confocal microscope (Olympus, USA).

4. Statistical analysis

Comparisons among groups were analyzed *via* independent samples with the one-factor ANOVA test using SPASS 17.0 software. All statistical data were obtained using a two-tailed student's *t* test and homogeneity of variance tests (p values < 0.05 were considered significant).

Conflict of interest

The authors declare no competing financial interest.

Acknowledgements

This work was supported by National Science Foundation of China (Grant No. 81571708, 81501506, 51373144 and 81201129), National High Technology Research and Development Program of China (863 Program) (Grant No. 2014AA020708), the Fundamental Research Funds for the Central Universities (Grant No. 20720150064), the Research Fund of Science and Technology Department of Jilin Province (Grant No. 20160101001JC), the Department of Education of Jilin Province for Thirteen-Five Scientific Technique Research (Grant No. [2016]460) and the Norman Bethune Program of Jilin University (Grant No. 2015219).

Appendix A. Supplementary data

Supplementary data related to this article can be found at http://dx.doi.org/10.1016/j.biomaterials.2016.10.030.

References

[1] W. Tang, Z. Zhen, M. Wang, H. Wang, Y. CHuang, W. Zhang, G. Wang, T. Todd, T. Cowger, H. Chen, L. Liu, Z. Li, J. Xie, Red blood cell-facilitated photodynamic therapy for Cancer treatment, Adv. Funct. Mater. 26 (2016) 1757–1768.
[2] R.L. Siegel, K.D. Miller, A. Jemal, Cancer statistics, 2015, CA Cancer J. Clin. 65 (2015) 5–29.
[3] Z. Gao, L. Zhang, Y. Sun, Nanotechnology applied to overcome tumor drug resistance, J. Control Release 162 (2012) 45–55.
[4] H.L. Lu, W.J. Syu, N. Nishiyama, K. Kataoka, P.S. Lai, Dendrimer phthalocyanine-encapsulated polymeric micelle-mediated photochemical internalization extends the efficacy of photodynamic therapy and overcomes drug-resistance in vivo, J. Control Release 155 (2011) 458–464.
[5] H.Y. Ding, H.J. Yu, Y. Dong, R.H. Tian, G. Huang, D.A. Boothman, et al., Photoactivation switch from type II to type I reactions by electron-rich micelles for improved photodynamic therapy of cancer cells under hypoxia, J. Control. Release 156 (2011) 276–280.
[6] M. Pineiro, A.M.D.R. Gonsalves, M.M. Pereira, S.J. Formosinho, L.G. Arnaut, New halogenated phenylbacteriochlorins and their efficiency in singlet-oxygen sensitization, J. Phys. Chem. A 106 (2002) 3787–3795.
[7] C. Zhang, K.L. Zhao, W.B. Bu, D.L. Ni, Y.Y. Liu, J.W. Feng, et al., Marriage of scintillator and semiconductor for synchronous radiotherapy and deep photodynamic therapy with diminished oxygen dependence, Angew. Chem. Int. Ed. 54 (2015) 1770–1774.
[8] J.J. Wang, L.W. Zhang, M.L. Chen, S. Gao, L. Zhu, Activatable ferritin nanocomplex for real-time monitoring of Caspase-3 activation during photodynamic therapy, Acs Appl. Mater. Inter. 7 (2015) 23248–23256.
[9] T.J. Dougherty, C.J. Gomer, B.W. Henderson, G. Jori, D. Kessel, M. Korbelik, et al., Photodynamic therapy, J. Natl. Cancer Inst. 90 (1998) 889–905.
[10] Z. Huang, H.P. Xu, A.D. Meyers, A.I. Musani, L.W. Wang, R. Tagg, et al., Photodynamic therapy for treatment of solid tumors - potential and technical challenges, Technol. Cancer Res. T 7 (2008) 309–320.
[11] J.M. Brown, W.R. Wilson, Exploiting tumour hypoxia in cancer treatment, Nat. Rev. Cancer 4 (2004) 437–447.
[12] M. Hockel, P. Vaupel, Tumor hypoxia: definitions and current clinical, biologic, and molecular aspects, J. Natl. Cancer I 93 (2001) 266–276.
[13] P. Vaupel, A. Mayer, Hypoxia in cancer: significance and impact on clinical outcome, Cancer Metast Rev. 26 (2007) 225–239.
[14] B.W. Henderson, V.H. Fingar, Relationship of tumor hypoxia and response to photodynamic treatment in an experimental mouse-tumor, Cancer Res. 47 (1987) 3110–3114.
[15] C.S. Jin, J.F. Lovell, J. Chen, G. Zheng, Ablation of hypoxic tumors with dose-equivalent photothermal, but not photodynamic, therapy using a nanostructured porphyrin assembly, Acs Nano 7 (2013) 2541–2550.
[16] J.B. Song, P. Huang, H.W. Duan, X.Y. Chen, Plasmonic vesicles of amphiphilic nanocrystals: optically active multifunctional platform for Cancer diagnosis and therapy, Accounts Chem. Res. 48 (2015) 2506–2515.
[17] M. Swierczewska, H.S. Han, K. Kim, J.H. Park, S. Lee, Polysaccharide-based nanoparticles for theranostic nanomedicine, Adv. Drug Deliv. Rev. 99 (2016) 70–84.
[18] K.T. Nguyen, Y. Zhao, Engineered hybrid nanoparticles for on-demand diagnostics and therapeutics, Acc. Chem. Res. 48 (2015) 3016–3025.
[19] S. Gao, L.W. Zhang, G.H. Wang, K. Yang, M.L. Chen, R. Tian, et al., Hybrid graphene/Au activatable theranostic agent for multimodalities imaging guided enhanced photothermal therapy, Biomaterials 79 (2016) 36–45.
[20] G. Wang, F. Zhang, R. Tian, L. Zhang, G. Fu, L. Yang, et al., Nanotubes-embedded indocyanine green-hyaluronic acid nanoparticles for photoacoustic-imaging-guided phototherapy, ACS Appl. Mater. Interfaces 8 (2016) 5608–5617.
[21] Z.P. Zhen, W. Tang, C.L. Guo, H.M. Chen, X. Lin, G. Liu, et al., Ferritin nanocages to encapsulate and deliver photosensitizers for efficient photodynamic therapy against Cancer, Acs Nano 7 (2013) 6988–6996.
[22] Z.H. Sheng, D.H. Hu, M.B. Zheng, P.F. Zhao, H.L. Liu, D.Y. Gao, et al., Smart human serum albumin-indocyanine green nanoparticles generated by programmed assembly for dual-modal imaging-guided Cancer synergistic phototherapy, Acs Nano 8 (2014) 12310–12322.
[23] G.R. Reddy, M.S. Bhojani, P. McConville, J. Moody, B.A. Moffat, D.E. Hall, et al., Vascular targeted nanoparticles for imaging and treatment of brain tumors, Clin. Cancer Res. 12 (2006) 6677–6686.
[24] J. Ge, M. Lan, B. Zhou, W. Liu, L. Guo, H. Wang, et al., A graphene quantum dot photodynamic therapy agent with high singlet oxygen generation, Nat. Commun. 5 (2014) 4596.
[25] J.Z. Zhao, W.H. Wu, J.F. Sun, S. Guo, Triplet photosensitizers: from molecular design to applications, Chem. Soc. Rev. 42 (2013) 5323–5351.
[26] W.M. Sharman, C.M. Allen, J.E. van Lier, Photodynamic therapeutics: basic principles and clinical applications, Drug Discov. Today 4 (1999) 507–517.
[27] H.C. Chen, J.W. Tian, W.J. He, Z.J. Guo, H2O2-Activatable and O-2-Evolving nanoparticles for highly efficient and selective photodynamic therapy

against hypoxic tumor cells, J. Am. Chem. Soc. 137 (2015) 1539–1547.
[28] W.W. Zhu, Z.L. Dong, T.T. Fu, J.J. Liu, Q. Chen, Y.G. Li, et al., Modulation of hypoxia in solid tumor microenvironment with MnO2 nanoparticles to enhance photodynamic therapy, Adv. Funct. Mater. 26 (2016) 5490–5498.
[29] Y.H. Cheng, H. Cheng, C.X. Jiang, X.F. Qiu, K.K. Wang, W. Huan, et al., Perfluorocarbon nanoparticles enhance reactive oxygen levels and tumour growth inhibition in photodynamic therapy, Nat. Commun. 6 (2015) 8785–8793.
[30] X. Song, L. Feng, C. Liang, K. Yang, Z. Liu, Ultrasound triggered tumor oxygenation with oxygen-shuttle nanoperfluorocarbon to overcome hypoxia-associated resistance in Cancer therapies, Nano Lett. 16 (2016) 6145–6153.
[31] P.T. Schumacker, Reactive oxygen species in cancer cells: live by the sword, die by the sword, Cancer Cell 10 (2006) 175–176.
[32] T.P. Szatrowski, C.F. Nathan, Production of large amounts of hydrogen-peroxide by human tumor-cells, Cancer Res. 51 (1991) 794–798.
[33] P. Prasad, C.R. Gordijo, A.Z. Abbasi, A. Maeda, A. Ip, A.M. Rauth, et al., Multifunctional albumin-MnO2 nanoparticles modulate solid tumor microenvironment by attenuating hypoxia, acidosis, vascular endothelial growth factor and enhance radiation response, Acs Nano 8 (2014) 3202–3212.
[34] C.R. Gordijo, A.Z. Abbasi, M.A. Amini, H.Y. Lip, A. Maeda, P. Cai, et al., Design of hybrid MnO2-polymer-lipid nanoparticles with tunable oxygen generation rates and tumor accumulation for Cancer treatment, Adv. Funct. Mater. 25 (2015) 1858–1872.
[35] S. Misra, P. Heldin, V.C. Hascall, N.K. Karamanos, S.S. Skandalis, R.R. Markwald, et al., Hyaluronan-CD44 interactions as potential targets for cancer therapy, Febs J. 278 (2011) 1429–1443.
[36] H. Jiang, R.S. Peterson, W.H. Wang, E. Bartnik, C.B. Knudson, W. Knudson, A requirement for the CD44 cytoplasmic domain for hyaluronan binding, pericellular matrix assembly, and receptor-mediated endocytosis in COS-7 cells, J. Biol. Chem. 277 (2002) 10531–10538.
[37] R.P. Huang, A. Peng, M.Z. Hossain, Y. Fan, A. Jagdale, A.L. Boynton, Tumor promotion by hydrogen peroxide in rat liver epithelial cells, Carcinogenesis 20 (1999) 485–492.
[38] T. Athar, N. Topnani, A. Hakeem, W. Ahmed, Synthesis and characterization of MnO_2 and CdO nanoparticles, Adv. Sci. Lett. 5 (2012) 1–4.
[39] J.Y. Zhu, J.H. He, Facile synthesis of graphene-wrapped honeycomb MnO2 nanospheres and their application in supercapacitors, Acs Appl. Mater. Inter. 4 (2012) 1770–1776.
[40] L.W. Zhang, S. Gao, F. Zhang, K. Yang, Q.J. Ma, L. Zhu, Activatable hyaluronic acid nanoparticle as a theranostic agent for optical/photoacoustic image-guided photothermal therapy, Acs Nano 8 (2014) 12250–12258.
[41] Y.L. Luo, Preparation of MnO2 nanoparticles by directly mixing potassium permanganate and polyelectrolyte aqueous solutions, Mater. Lett. 61 (2007) 1893–1895.
[42] Y. Kato, S. Ozawa, C. Miyamoto, Y. Maehata, A. Suzuki, T. Maeda, et al., Acidic extracellular microenvironment and cancer, Cancer Cell Int. 13 (2013) 89–97.
[43] E.K. Rofstad, B. Mathiesen, K. Kindem, K. Galappathi, Acidic extracellular pH promotes experimental metastasis of human melanoma cells in athymic nude mice, Cancer Res. 66 (2006) 6699–6707.
[44] K.Y. Choi, K.H. Min, H.Y. Yoon, K. Kim, J.H. Park, I.C. Kwon, et al., PEGylation of hyaluronic acid nanoparticles improves tumor targetability in vivo, Biomaterials 32 (2011) 1880–1889.
[45] D.E.J.G.J. Dolmans, D. Fukumura, R.K. Jain, Photodynamic therapy for cancer, Nat. Rev. Cancer 3 (2003) 380–387.
[46] M.E. Milanesio, M.G. Alvarez, V. Rivarola, J.J. Silber, E.N. Durantini, Porphyrin-fullerene C-60 dyads with high ability to form photoinduced charge-separated state as novel sensitizers for photodynamic therapy, Photochem. Photobiol. 81 (2005) 891–897.
[47] M. Pineiro, M.M. Pereira, A.M.D.R. Gonsalves, L.G. Arnaut, S.J. Formosinho, Singlet oxygen quantum yields from halogenated chlorins: potential new photodynamic therapy agents, J. Photochem. Photobiol. A 138 (2001) 147–157.
[48] W.O. Carter, P.K. Narayanan, J.P. Robinson, Intracellular hydrogen peroxide and superoxide anion detection in endothelial cells, J. Leukoc. Biol. 55 (1994) 253–258.
[49] K.Y. Choi, H. Chung, K.H. Min, H.Y. Yoon, K. Kim, J.H. Park, et al., Self-assembled hyaluronic acid nanoparticles for active tumor targeting, Biomaterials 31 (2010) 106–114.
[50] M.L. Song, T. Liu, C.R. Shi, X.Z. Zhang, X.Y. Chen, Bioconjugated manganese dioxide nanoparticles enhance chemotherapy response by priming tumor-associated tL.A macrophages toward m1-like phenotype and 11 attenuating tumor hypoxia (vol 10, pg 633, 2016), Acs Nano 10 (2016), 3872-3872.